Current Optics and Photonics
Vol. 5, No. 6, December 2021, pp. 652–659

ISSN: 2508-7266(Print) / ISSN: 2508-7274(Online)
DOI: https://doi.org/10.3807/COPP.2021.5.6.652

Theoretical Analysis and Optimization of Extrinsic Fabry-Perot Interferometer Optical-fiber Humidity-sensor Structures

Xiao Lei Yin, Ning Wang*, Xiao Dan Yu, Yu Hao Li, Bo Zhang, and Dai Lin Li

College of Science, China University of Petroleum (Huadong), Qingdao 266580, China

(Received July 29, 2021 : revised September 7, 2021 : accepted September 15, 2021)

The theoretical analysis and optimization of extrinsic Fabry-Perot interferometer (EFPI) optical-fiber humidity sensors are deeply investigated. For a typical dual-cavity structure composed of an optical fiber and a humidity-sensitive membrane (HSM), the changes in refractive index (RI) and initial length are discussed for polymer materials and porous oxide materials when relative humidity (RH) increases. The typical interference spectrum is simulated at different RH using MATLAB. The spectral change caused by changing HSM RI and initial length are simulated simutineously, showing different influences on humidity response. To deeply investigate the influence on RH sensitivity, the typical response sensitivity curves for different HSM lengths and air-cavity lengths are simulated. The results show that the HSM is the vital factor. Short HSM length can improve the sensitivity, but for HSM RI and length the influences on sensitivity are opposite, because of the opposite spectral-shift trend. Deep discussion and an optimization method are provided to solve this problem. According to analysis, an opaque HSM is helpful to improve sensitivity. Furthermore, if using an opaque HSM, a short air cavity and long HSM length can improve the sensor's sensitivity These results provide deep understanding and some ideas for designing and optimizing highly sensitive EFPI fiber humidity sensors.

Keywords : Extrinsic Fabry-Perot interferometer, Humidity responding sensitivity, Optical fiber humidity sensor, Optimization, Theoretical simulation
OCIS codes : (060.2310) Fiber optics; (060.2370) Fiber optics sensors; (120.2230) Fabry-Perot

I. INTRODUCTION

Compared to a traditional electronic humidity sensor, optical-fiber humidity sensors are superior in many ways, such as miniature size, flexible measurement, freedom from electromagnetic interference, and high precision, and they have great potential for application in the semiconductor industry [1], clinical medicine [2], leakage detection [3], and high-energy physics [4]. The extrinsic Fabry-Perot interferometer (EFPI) sensor is a typical kind of optical-fiber humidity sensors, with a simple principle, convenient demodulation, and diversified structures. Usually by combining an optical fiber with a humidity-sensitive membrane (HSM), the EFPI sensor uses the fiber's end and HSM film as reflection surfaces to form the Fabry-Perot (F-P) cavities. The HSM interacts with water molecules and directly influences the F-P cavity's parameters, so the environment's relative humidity (RH) can be measured by the interference spectrum.

In recent years, a hot topic in EFPI optical-fiber humidity sensors is the use of a capillary tube or special optical fiber, including hollow-core fiber (HCF) [5–7], hollow-core photonic crystal fiber (HCPFC) [8], and microstructured optical fiber (MOF) [9, 10]. Through these elements, an interference structure with two cascaded F-P cavities can be constituted. In 2016, Liu *et al*. [8] fused a section of HCPCF with a single-mode fiber (SMF), and formed chitosan film on the other end of a HCPFC to build an EFPI sensor, obtaining 0.28 nm/%RH sensitivity in the RH range from 35% to 95%. In 2017, Aldaba *et al*. [9] sputtered SnO_2 film

*Corresponding author: qfwangning@163.com, ORCID 0000-0003-1392-3835
Color versions of one or more of the figures in this paper are available online.

on the lining of a MOF, and fused it to an SMF, obtaining 0.14 rad/%RH sensitivity at 20%–90% RH with this sensor. In 2018, Li *et al*. [11] presented an EFPI sensor with a capillary tube between the SMF and a graphene oxide (GO) diaphragm, with a sensitivity of 0.2 nm/%RH in the RH range from 10% to 90%. In the same year, Bian *et al*. [6] fabricated an EFPI sensor combining SMF with HCF and polyimide (PI); this sensor reached a high sensitivity of 1.309 nm/%RH in the 40% to 80% RH range. Using a similar structure to Bian's, in 2019 Zhao *et al*. [5] adopted the widely used graphene and polyvinyl alcohol (PVA) as a humidity-sensitive material [12–14], and got 117.25 pm/%RH sensitivity from 13.47%RH to 81.34%RH. In 2020, Shrivastav *et al*. [10] utilized MOF and chitosan to form a sensing probe, with a maximum sensitivity of 81.05 pm/%RH in the range of 90–95%RH. The above sensors with different structures and HSMs show remarkable sensitivity differences, which is related to HSM selection and sensor structure. Many reports have obtained good humidity-measurement results with their sensor structures, but less attention has been paid to deeply investigating and analyzing the influential factors of the sensitivity characteristic, by simulation and analysis. Deep investigation can give more ideas for optimizing sensor structure and improving the response sensitivity of an EFPI humidity sensor.

In this paper, simulation and optimization of an EFPI optical-fiber humidity sensor in its sensing characteristics are investigated. The course of water-molecule absorption of the HSM is analyzed. For polymer HSMs and porous oxide materials, the refractive index (RI) and volume change are discussed. For a typical dual-cavity structure, the interference spectrum is simulated and analyzed at different RH, especially the influence on response sensitivity caused by the change of HSM RI and cavity length. Furthermore, the humidity sensitivity changes caused by HSM initial length and air-cavity initial length are deeply investigated, and show obviously different results. The simulation results also show that for the changes in HSM RI and length, the influences on humidity response sensitivity are opposite. Then the method of humidity response sensitivity optimization is deeply discussed, including how to eliminate the opposite spectrum-shift effect. The research results give deep understanding of EFPI humidity-sensor response characteristics and clear methods for sensitivity optimization. The simulations and analysis are very helpful to deeply understand and optimize EFPI optical-fiber humidity sensors.

II. EFPI SENSING STRUCTURES AND PRINCIPLE

According to the EFPI sensor's principle of operation, whether using special fiber or capillary tube, the reported EFPI optical-fiber humidity sensors can be summed up as one structure, as shown in Fig. 1. The SMF-air-HSM structure is an interference structure with two F-P cavities. The light is reflected at three interfaces of SMF, air, and HSM, and the interference spectrum is the result of coherent superposition of the three reflected beams.

The first interference cavity is an air cavity, and the second interference cavity is the HSM. Assuming that the length and RI of these two interference cavities are d_1 and d_2 and n_1 and n_2 respectively, and that generally $n_1 = 1$, the normalized reflected light intensity of the SMF-air-HSM sensor can be expressed as

$$\begin{aligned} I = {} & R_1 + R_2(1-R_1)^2 + (1-R_1)^2(1-R_2)^2 R_3 \\ & + 2\sqrt{R_1 R_3}(1-R_1)(1-R_2)\cos(\delta_1+\delta_2) \\ & + 2\sqrt{R_2 R_3}(1-R_1)^2(1-R_2)\cos(\delta_2) + 2\sqrt{R_1 R_2}(1-R_1)\cos(\delta_1), \end{aligned} \tag{1}$$

where R_1, R_2, and R_3 are respectively the reflectivity of the SMF/air interface, air/HSM interface, and HSM/air interface, and $\delta_1 = \frac{4\pi n_1 d_1}{\lambda}$ and $\delta_2 = \frac{4\pi n_2 d_2}{\lambda}$ are respectively the phase difference between reflected beams of the two interference cavities.

When the RH of the environment increases, the interaction between the HSM and water molecules will lead to variation of the parameters of the F-P cavity, resulting in a change in the optical-path difference of the reflection beams. For each F-P cavity, the change in optical-path difference can be expressed as

$$\Delta L = 2(\Delta n d + n\Delta d) = L\left(\frac{\Delta n}{n} + \frac{\Delta d}{d}\right), \tag{2}$$

where $L = 2nd$, which is the initial optical-path difference between two adjacent reflection beams. d and n are respectively the initial cavity length and RI of HSM (or air), and Δn and Δd are the RI changes and cavity length change caused by the RH. The HSM change caused by RH leads to change in the interference effects of the two cavities. The coherent-superposition light intensity also changes. Thus the HSM change is the vital factor in the dual-cavity structure.

Up to now, the reported HSM materials in EFPI optical-fiber humidity sensors include PVA [15, 16], PI [6, 17], agar [18], chitosan [8, 10], nafion [19, 20], GO [11, 21], graphene quantum dots (GQDs) [22], porous anodic alumina (PAA) [23], tin dioxide (SnO_2) [9], polyvinylidene fluoride (PVDF) [24], cellulose acetate butyrate (CAB) [25], PVA-GQD compounds [5], carboxymethylcellulose/carbon nanotubes (CMC/CNTs) compounds [7], poly(allylamine

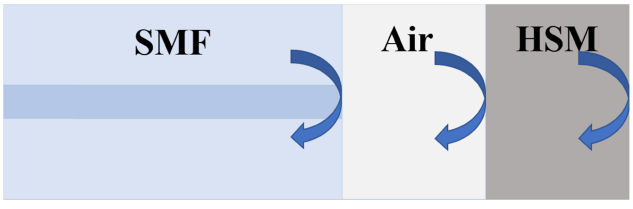

FIG. 1. Extrinsic Fabry-Perot interferometer (EFPI) humidity-sensing structure.

hydrochloride)/silica (PAH/SiO_2) compounds [2], porous TiO_2/SiO_2/TiO_2 compounds [26, 27], poly(allylamine hydrochloride)/poly(sodium-p-styrene sulfonate) (PAH/PSS) compounds [28], and more. These polymers, porous oxides and complexes usually contain a large number of hydrophilic groups, or have a high porosity, to ensure the adsorption of water molecules. When these materials interact with the water molecules, their volume or RI changes, and the changes leads to variations in peak position and intensity of the sensor's interference spectrum. This is the RH measurement basis of an EFPI optical-fiber humidity sensor.

The interaction of polymers, graphene materials, or their complexes with water molecules can be explained by the analysis of Zhao *et al*. [17]. Zhao *et al*. [17] divided the water molecules affecting the parameter of HSM into two categories: the first was liquid water occupying the pores in the HSM, and the second was the water gathered in the molecular clusters of hydrophilic substances in the HSM. The second type of water molecules enter the HSM and take up additional space, resulting in the volume expansion of the HSM. Assuming the volume fractions of the first and second water molecules are ϕ_1 and ϕ_2 respectively, the volume of the HSM in adsorption equilibrium can be expressed as

$$V = \frac{V_0}{1 - \phi_2}, \tag{3}$$

where V_0 is the initial volume of the HSM. Due to the limited pores in a polymer material, the adsorption of the first water molecules on a humidity-sensitive material soon reaches saturation, and then the HSM continues to adsorb the second type of water molecules until dynamic equilibrium between the water molecules and the HSM is established. With higher external RH, the volume fraction of the second type of water molecules (ϕ_2) is greater. Thus it can be seen from Eq. (3) that with the increase of environmental RH, the volume of the HSM will gradually increase, due to the increase in the content of water molecules. In addition, the effective RI of the HSM after adsorption equilibrium can be expressed as

$$n_{\text{eff}} = n + (n_{\text{water}} - 1)\phi_1 + (n_{\text{water}} - n)\phi_2, \tag{4}$$

where n is the initial RI of HSM, and n_{water} is the RI of water. The initial RI of such materials is generally higher than that of water, which means $(n_{\text{water}} - n) < 0$. It can be understood from Eq. (4) that with the increase of water-molecule content of the HSM, the effective RI of the material will show a downward trend. In fact, some reported results, such as the RI changes of PVA [29], agar [30], chitosan [31], and GQDs [5], also support this conclusion. Thus with increased water-molecule absorption, for polymer materials, graphene materials, or their complexes, $\Delta n < 0$ and $\Delta d > 0$, where Δn and Δd are respectively the RI change and length change of the HSM.

The moisture absorption of a porous oxide is mainly realized by capillary condensation due to the pore structure. When the adsorption of environmental water molecules is stable, the effective RI of a porous oxides approximately obeys the following equation [27]:

$$(1-f)\frac{n_{\text{oxide}}^2 - n_{\text{eff}}^2}{n_{\text{oxide}}^2 + 2n_{\text{eff}}^2} + (f-\phi)\frac{n_{\text{air}}^2 - n_{\text{eff}}^2}{n_{\text{air}}^2 + 2n_{\text{eff}}^2} + \phi\frac{n_{\text{water}}^2 - n_{\text{eff}}^2}{n_{\text{water}}^2 + 2n_{\text{eff}}^2} = 0, \tag{5}$$

here f is the porosity of the oxide, ϕ is the volume fraction of condensed water in the porous oxide, and n_{oxide}, n_{air}, and n_{water} is the RI of oxide, air, and water respectively. Generally we take $n_{\text{air}} = 1$ and $n_{\text{water}} = 1.33$.

By solving Eq. (5), the relationship between the effective RI of a porous oxide and volume fraction of water in the oxide can be obtained. Figure 2 shows the typical simulation curves for the RI of porous alumina with varying water content. We can see that there is a good linear relationship between RI and ϕ, and the slope of the lines is 0.3504, 0.3459, 0.3415 and 0.3372 when the porosity f is 0.5, 0.6, 0.7, and 0.8 respectively. It can be shown that change trend of a porous oxide's effective RI with different porosity is basically similar. All curves show that the effective RI well linearly increases with the increasing volume fraction of water, and with higher porosity, the overall effective RI of a porous oxide is lower. So, for porous oxide materials, with the increased water-molecule absorption, RI increases ($\Delta n > 0$, where Δn is the RI change value). According to some reports on EFPI optical-humidity sensors fabricated from porous oxide, the humidity response caused by porous oxide is mainly related to the HSM's RI [23, 26], so we just discuss the influence of RI.

III. SIMULATION RESULTS AND DISSCUSSION

The SMF-air-HSM structure has two F-P interference

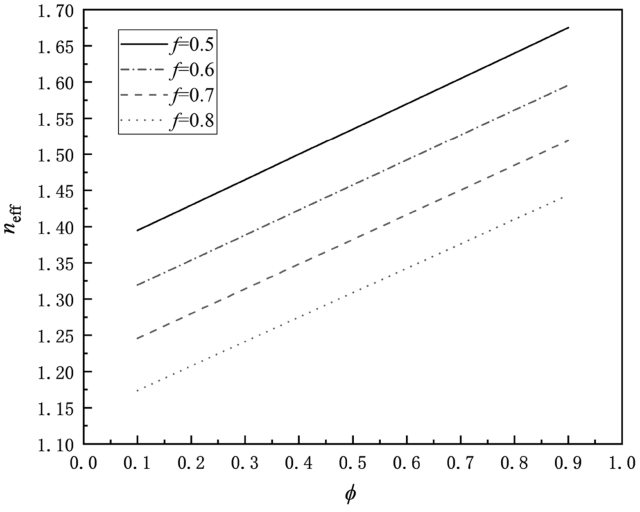

FIG. 2. Change in porous alumina's effective refractive index (RI) changes with changing volume fraction of water molecules.

areas: the air and HSM areas. According to the analysis results above, the interference spectrum of a dual-cavity structure can be simulated. Most of the reported SMF-air-HSM structure have used polymer or graphene materials for the HSM. In this paper, we also use this kind of HSM for simulation. Assuming that the HSM linearly expands, we take the typical expansion coefficient of chitosan (equal to 0.3321, which is calculated from [31]) and the RI of PVA in [32] as data references. The interference spectra of sensors with different parameters can be simulated by MATLAB software. The typical length of the HSM is 10 μm, and the length of the air cavity in the SMF-air-HSM structure is 100 μm. Figure 3 shows the simulated interference spectra. The interference spectrum of an SMF-air-HSM sensor is a series of envelope waveforms with different contrasts, because of the dual-cavity structure. We simulate three interference-spectrum curves, at 40%, 50%, and 60%RH. The spectrum shows a red-shift when the environmental RH increases, but the overall contrast of the spectral line is almost unchanged.

As per analysis of a polymer HSM, the RI change and HSM length change caused by RH are opposite. To investigate the influence of these two parameters in depth, simulations with various lengths or RIs, are both performed. Figure 4 shows the interference-spectrum changes with changing material length and RI. The RH value still changes from 40% RH to 50%RH. It can be seen that the interference spectrum shifts to red as the length increases, and shifts to blue as the RI decreases. The peak wavelength shift caused by increasing material length is about 58.692 nm, and the peak wavelength shift caused by decreasing material RI is about 10.414 nm. So the spectral shift caused by HSM length variation is usually greater than that due to RI variation. In fact, the interference spectra of reported EFPI humidity sensors adopting polymer or graphene materials or their complexes for the HSMs are almost all consistent with this conclusion.

According to the former discussion, with increasing RH the HSM's RI value decreases and the HSM's length increases. This means that for RI and HSM length the influences on humidity-response sensitivity are opposite, because of the opposite spectrum-shift trend when RH increases. This effect can deteriorate humidity-response sensitivity, but also provides a key point for optimizing sensor sensitivity. The optimization analysis will be carried out later.

Cavity length, which is the main factor affecting the phase difference between the two adjacent beams of an EFPI sensor, is directly related to the sensor's sensitivity. To deeply investigate the influence of cavity length, more simulations are performed.

For the sake of discussion, the sensor's sensitivity is characterized by the shift of the peak position near 1550 nm (as a typical value) when the RH increases from 40% to 50%. Assuming that the air cavity's initial length is 100 μm, and setting the length of the HSM to 5, 10, 15, 20, 25, 30, 35, and 40 μm, the interference spectra under different conditions are simulated yielding the spectral shifts for different HSM lengths. The sensitivity is also obtained from the results. The relationship between the length of the HSM and the sensor's sensitivity can be obtained, as shown in Fig. 5(a). There is a good, linear inverse relationship between the initial length of the HSM and sensitivity, and a sensitivity of 0.0288 nm/%RH decrease per 1 μm of length increase is obtained. Thus reducing the HSM's length can increase the sensitivity of an SMF-air-HSM sensor, for a certain air-cavity length. By the same method, we also deeply investigate the influence on sensitivity caused by the cavity's initial length, and find the simulation curve seen in Fig. 5(b), where the length of the HSM is 10 μm, and the length of the air cavity varies in steps of from 60 to 200 μm. As Fig. 5(b) shows, the sensitivity fluctuates slightly

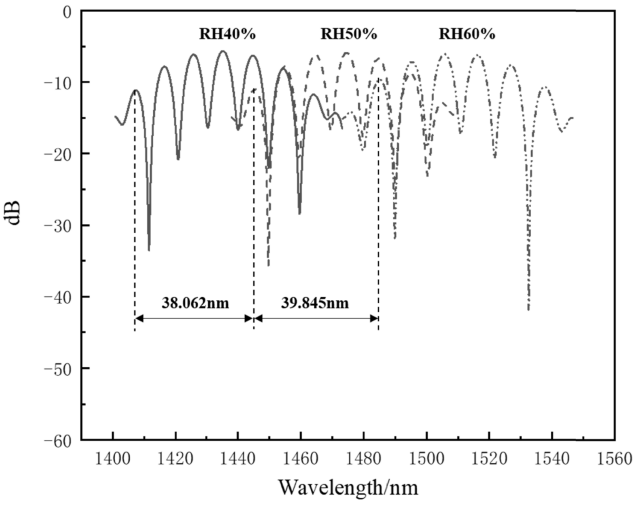

FIG. 3. Interference spectra of an single-mode fiber-air-humidity-sensitive membrane (SMF-air-HSM) sensor.

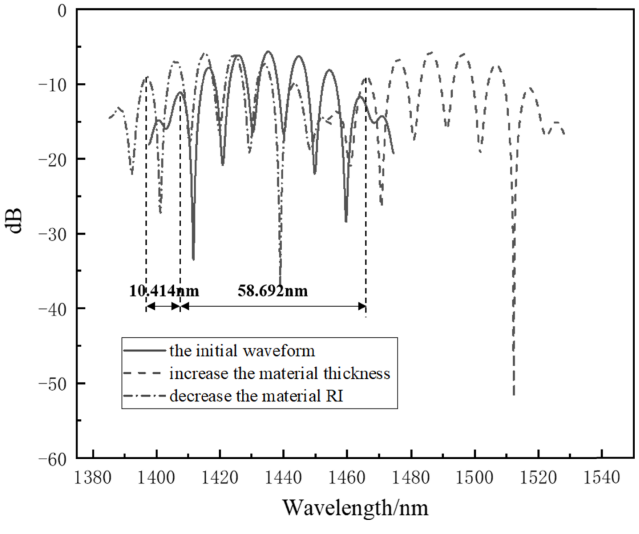

FIG. 4. Spectral change caused by change in material initial length and refractive index (RI).

around 4.28 nm/%RH with increasing length of the air cavity, and its sensitivity increases or decreases by about 0.0408 nm/%RH for per 1 μm of change in the initial length of the air cavity, which means the sensitivity fluctuation caused by air cavity is approximately ± 0.0408 (nm/%RH)/μm. Thus the influence of the air cavity on sensitivity seems to be not obvious, on the whole. With varied air-cavity initial length, the sensitivity is nearly unchanged.

IV. STRUCTURE OPTIMIZATION AND ANALYSIS

According to the previous analysis, it seems that short HSM initial length is good for improving the sensor's humidity sensitivity. This is one optimization method. To further investigate sensitivity improvement, we next provide another method of optimizing the structure.

As in the earlier analysis of the SMF-air-HSM structure sensor, when the RH of the environment increases, the length of the first interference cavity decreases, due to the expansion of the HSM, while the length of the second interference cavity increases but the cavity's RI decreases. These changes lead to the wavelength shift of the interference spectrum as a whole. But for RI and length of HSM, the influence on humidity-response sensitivity is opposite. This is not good for improving sensitivity. However, if the HSM is opaque, light beams do not interfere in the second cavity formed by the HSM. The F-P interference is attained only by the air cavity of the SMF-air-HSM EFPI sensor, as Fig. 6 shows. Therefore, the opposite effects on sensor sensitivity caused by HSM RI reduction and hygroscopic expansion can be avoided. The optimized structure is showed in Fig. 6.

For this structure the sensitivity expression is deduced as [18]

$$\frac{\Delta\lambda}{\Delta \mathrm{RH}} = \lambda \frac{1}{d_1} \frac{\Delta d_2/2}{\Delta \mathrm{RH}}, \tag{6}$$

in which d_1 is the length of the air cavity, and Δd_2 is the amount of expansion of the HSM. To investigate the effect of structure optimization, we simulate the response curves, and get the wavelength shift for different air-cavity initial lengths, as Fig. 7 shows. The air cavity's initial length takes on values of 100, 80, 60, 40, and 20 μm. For an ambient humidity change from 20%RH to 21%RH as typical values, the HSM lengths are 48.93 and 49 μm, and the RIs are 1.4666 and 1.465, respectively.

According to Fig. 7, after optimization, the wavelength-shift values are 0.444 nm, 0.65 nm, 0.821 nm, 1.403 nm and 2.804 nm respectively. Obviously the sensitivity of the optimized sensor structure is greatly improved, because of the bigger wavelength-shift values. For example, the wavelength shift for 20-μm air-cavity initial length is 9 times that of the unoptimized sensor. In addition, Fig. 7 also shows that reducing the length of the air cavity can further increase the sensitivity of the sensor after optimization, which conforms to Eq. (6). It is interesting to note that if using this optimized sensor structure, a long HSM

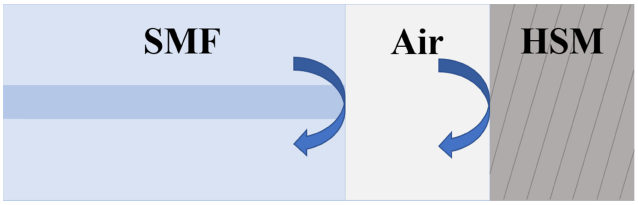

FIG. 6. Optimized structure for an extrinsic Fabry-Perot interferometer (EFPI) sensor structure.

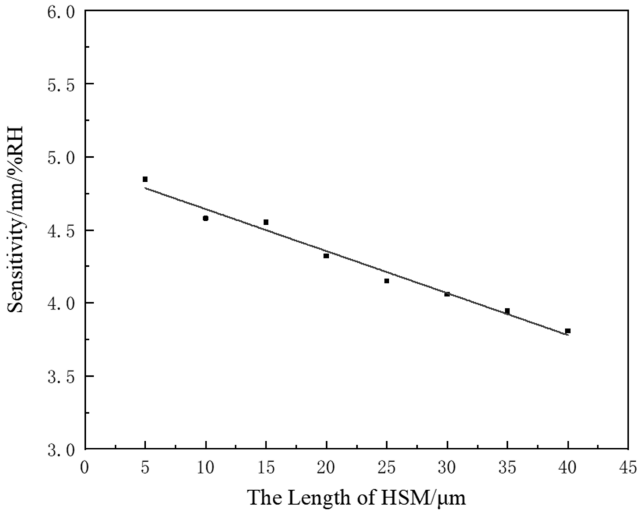

(a)

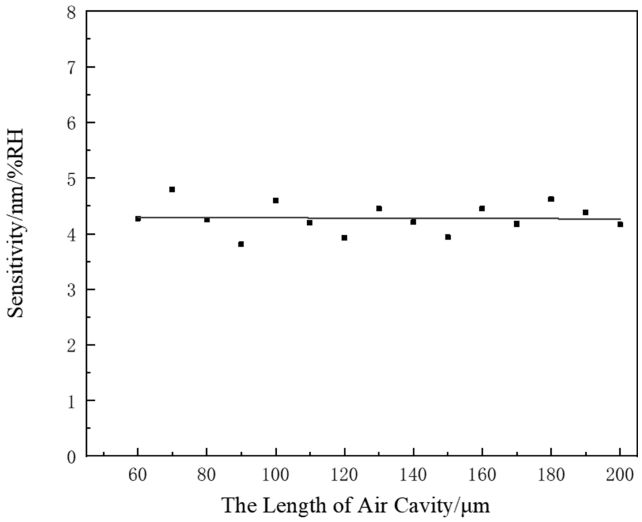

(b)

FIG. 5. Change in sensitivity of an single-mode fiber-air-humidity-sensitive membrane (SMF-air-HSM) sensor, caused by (a) the initial length of the HSM, and (b) the initial length of the air cavity.

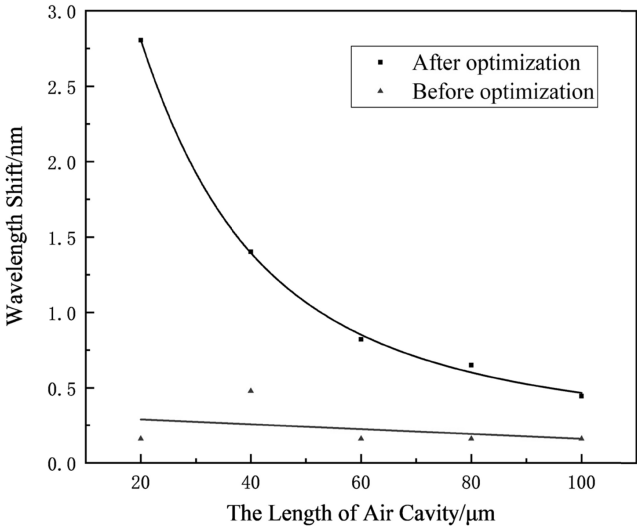

FIG. 7. Wavelength shift for different air-cavity initial length.

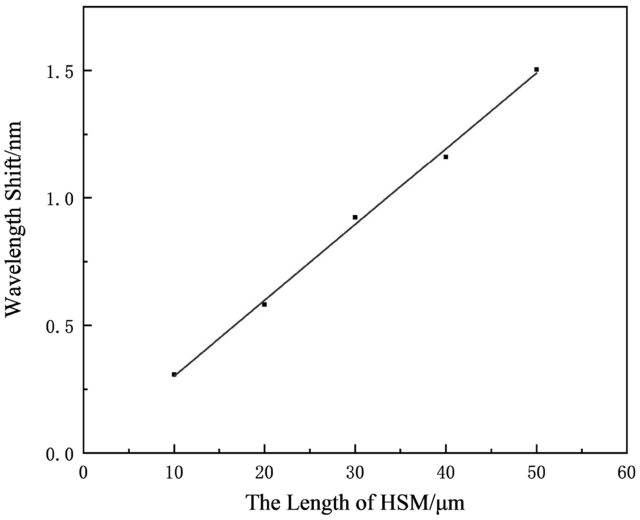

FIG. 8. Wavelength shift for different humidity-sensitive membrane (HSM) initial length in an optimizing sensor.

length is helpful to improve the sensitivity according to the simulation results of Fig. 8. This is opposite to the situation for an unoptimized sensor. In Fig. 8, the typical initial air-cavity length is 50 μm, and the HSM initial length takes on values of 10, 20, 30, 40, and 50 μm. The RH value also changes from 20% to 21% as before. We can see that higher wavelength shift is attained with larger HSM length. Because large HSM length can lead to high expansion of the HSM, which means large Δd_2 in Eq. (6), the sensitivity is improved.

Thus by the former analysis, we obtain methods to optimize an EFPI humidity sensor's structure: using a short or opaque HSM. If using an opaque HSM, a short air-cavity length, and long HSM are helpful to further improve humidity-response sensitivity.

V. CONCLUSION

In this paper, the theoretical analysis and optimization of the sensing characteristics of an EFPI optical-fiber humidity sensor have been deeply investigated. The typical dual-cavity structure, namely an SMF-air-HSM structure, consists of a cascade of air cavity and HSM. Typical interference spectra were simulated at different RH levels, and the spectral changes were also simulated when HSM thickness and RI were changed. For HSM RI and HSM length, the influences on humidity-response sensitivity are opposite. To deeply investigate the influence on sensitivity, curves were simulated with different HSM initial lengths and air-cavity initial lengths. According to these simulations, the length of the air cavity is not the key factor affecting the sensor's sensitivity, but the length of the HSM obviously affects the sensitivity for a certain length of air cavity. Avoiding the interference in the HSM can eliminate the opposite effects of HSM RI reduction and hygroscopic expansion on sensor sensitivity, so that the sensing performance is greatly improved.

The optimization discussion of humidity-sensing characteristics was conducted from the cavity-length aspect and structure aspect. Different form well-known optimization methods, such as choosing a more sensitive material, our analysis showed that using a short opaque HSM can be effective for improving humidity sensitivity. If using an opaque HSM, a short air cavity and long HSM are also helpful to further improve sensitivity. The typical optimization sensitivity curves were simulated and analyzed, and the results showed obvious sensitivity improvement.

Of course, the experimental improvement of sensor sensitivity is also related to other actual factors, such as the fabrication process, actual response characteristics of the HSM, and other factors in a practical application environment. In this paper, by the theoretical analysis and optimization discussion we simply wanted to provide some understanding of the sensing characteristics and optimization ideas for EFPI optical-fiber humidity sensors, which is helpful in designing and manufacturing highly sensitive sensors. In the future some experiments will be conducted to confirm our conclusion.

ACKNOWLEDGMENT

This study was supported by the National Natural Science Foundation of China (No. 61805285), the Graduate Innovation Engineering Project (YCX2020118), and the National Training Program of Innovation and Entrepreneurship for Undergraduates (Nos. 202012047).

REFERENCES

1. S. A. Kolpakov, N. T. Gordon, C. Mou, and K. Zhou, "Toward a new generation of photonic humidity sensors," Sensors **14**, 3986–4013 (2014).

2. F. U. Hernandez, S. P. Morgan, B. R. Hayes-Gill, D. Harvey, W. Kinnear, A. Norris, D. Evans, J. G. Hardman, and S. Korposh, "Characterization and use of a fiber optic sensor based on PAH/SiO_2 film for humidity sensing in ventilator care equipment," IEEE Trans. Biomed. Eng. **63**, 1985–1992 (2016).
3. H. J. Kim, H. Y. Shin, C. H. Pyeon, S. Kim, and B. Lee, "Fiber-optic humidity sensor system for the monitoring and detection of coolant leakage in nuclear power plants," Nucl. Eng. Technol. **52**, 1689–1696 (2020).
4. G. Berruti, M. Consales, M. Giordano, L. Sansone, P. Petagna, S. Buontempo, G. Breglio, and A. Cusano, "Radiation hard humidity sensors for high energy physics applications using polyimide-coated fiber Bragg gratings sensors," Sens. Actuators B Chem. **177**, 94–102 (2013).
5. Y. Zhao, R. J. Tong, M. Q. Chen, and F. Xia, "Relative humidity sensor based on hollow core fiber filled with GQDs-PVA," Sens. Actuators B Chem. **284**, 96–102 (2019).
6. C. Bian, M. Hu, R. Wang, T. Gang, R. Tong, L. Zhang, T. Guo, X. Liu, and X. Qiao, "Optical fiber humidity sensor based on the direct response of the polyimide film," Appl. Opt. **57**, 356–361 (2018).
7. J. Li, J. Zhang, H. Sun, Y. Yang, and Y. Xie, "An optical fiber sensor based on carboxymethyl cellulose/carbon nanotubes composite film for simultaneous measurement of relative humidity and temperature," Opt. Commun. **467**, 125740–125747 (2020).
8. X. Liu, M. Jiang, Q. Sui, and X. Geng, "Optical fibre Fabry–Perot relative humidity sensor based on HCPCF and chitosan film," J. Mod. Opt. **63**, 1668–1674 (2016).
9. A. L. Aldaba, D. Lopez-Torres, C. Elosua, J.-L. Auguste, R. Jamier, P. Roy, F. J. Arregui, and M. Lopez-Amo,"SnO_2-MOF-Fabry-Perot optical sensor for relative humidity measurements," Sens. Actuators B Chem. **257**, 189–199 (2018).
10. A. M. Shrivastav, D. S. Gunawardena, Z. Y. Liu, and H.-Y. Tam, "Microstructured optical fiber based Fabry–Pérot interferometer as a humidity sensor utilizing chitosan polymeric matrix for breath monitoring," Sci. Rep. **10**, 6002 (2020).
11. C. Li, X. Yu, W. Zhou, Y. Cui, J. Liu, and S. Fan, "Ultrafast miniature fiber-tip Fabry–Perot humidity sensor with thin graphene oxide diaphragm," Opt. Lett. **43**, 4719–4722 (2018).
12. P. Sun, M. Wang, L. Liu, L. Jiao, W. Du, F. Xia, M. Liu, W. Kong, L. Dong, and M. Yun, "Sensitivity enhancement of surface plasmon resonance biosensor based on graphene and barium titanate layers," Appl. Surf. Sci. **475**, 342–347 (2019).
13. H. Feng, Z. Xu, K. Li, M. Wang, W. Xie, Q. Luo, B. Chen, W. Kong, and M. Yun, "Tunable polarization-independent and angle-insensitive broadband terahertz absorber with graphene metamaterials," Opt. Express **29**, 7158–7167 (2021).
14. H. Feng, X. Li, M. Wang, F. Xia, K. Zhang, W. Kong, L. Dong, and M. Yun, "Ultrabroadband metamaterial absorbers from ultraviolet to near-infrared based on multiple resonances for harvesting solar energy," Opt. Express **29**, 6000–6010 (2021).
15. D. Su, X. Qiao, Q. Rong, H. Sun, J. Zhang, Z. Bai, Y. Du, D. Feng, Y. Wang, M. Hu, and Z. Feng, "A fiber Fabry–Perot interferometer based on a PVA coating for humidity measurement," Opt. Commun. **311**, 107–110 (2013).
16. M.-Q. Chen, Y. Zhao, H.-M. Wei, C.-L. Zhu, and S. Krishnaswamy, "3D printed castle style Fabry-Perot microcavity on optical fiber tip as a highly sensitive humidity sensor," Sens. Actuators B Chem. **328**, 128981 (2021).
17. Y. Zhao, Y. Yuan, W. Gan, and M. Yang, "Optical fiber Fabry–Perot humidity sensor based on polyimide membrane: sensitivity and adsorption kinetics," Sens. Actuators A Phys. **281**, 48–54 (2018).
18. B. Wang, J. Tian, L. Hu, and Y. Yao, "High sensitivity humidity fiber-optic sensor based on all-agar Fabry–Perot interferometer," IEEE Sens. J. **18**, 4879–4885 (2018).
19. J. S. Santos, I. M. Raimundo Jr, C. M. B. Cordeiro, C. R. Biazoli, C. A. J. Gouveia, and P. A. S. Jorge, "Characterisation of a Nafion film by optical fibre Fabry–Perot interferometry for humidity sensing," Sens. Actuators B Chem. **196**, 99–105 (2014).
20. S. Liu, Y. Ji, J. Yang, W. Sun, and H. Li,, "Nafion film temperature/humidity sensing based on optical fiber Fabry-Perot interference," Sens. Actuators A Phys. **269**, 313–321 (2018).
21. C. Li, X. Yu, T. Lan, J. Liu, and S. Fan, "Insensitivity to humidity in Fabry–Perot sensor with multilayer graphene diaphragm," IEEE Photonics Technol. Lett. **30**, 565–568 (2018).
22. N. Wang, W. Tian, H. Zhang, X. Yu, X. Yin, Y. Du, and D. Li, "An easily fabricated high performance Fabry-Perot optical fiber humidity sensor filled with graphene quantum dots," Sensors **21**, 806 (2021).
23. C. Huang, W. Xie, M. Yang, J. Dai, and Z. Bo, "Optical fiber Fabry–Perot humidity sensor based on porous Al_2O_3 film," IEEE Photonics Technol. Lett. **27**, 2127–2130 (2015).
24. A. Vaz, N. Barroca, M. Ribeiro, A. Pereira, and O. Frazão, "Optical fiber humidity sensor based on polyvinylidene fluoride Fabry–Perot," IEEE Photonics Technol. Lett. **31**, 549–552 (2019).
25. X. Wei, W. B. Huang, X. G. Huang, and C. Y. Yu, "A simple fiber-optic humidity sensor based on extrinsic Fabry–Perot cavity constructed by cellulose acetate butyrate film," Opt. Fiber Technol. **19**, 583–586 (2013).
26. M. Yang, W. Xie, Y. Dai, D. Lee, J. Dai, Y. Zhang, and Z. Zhuang, "Dielectric multilayer-based fiber optic sensor enabling simultaneous measurement of humidity and temperature," Opt. Express **22**, 11892–11899 (2014).
27. C. Huang, W. Xie, D. Lee, C. Qi, M. Yang, M. Wang, and J. Tang, "Optical fiber humidity sensor with porous TiO_2/SiO_2/TiO_2 coatings on fiber tip," IEEE Photonics Technol. Lett. **27**, 1495–1498 (2015).
28. Q. Sui, M. Jiang, Z. Jin, F. Zhang, Y. Cao, and L. Jia, "Optical fiber relative humidity sensor based on Fabry-Perot interferometer coated with sodium-p-styrenesulfonate/allylamine hydrochloride films," Sens. Mater. **26**, 291–298 (2014).
29. Y. Miao, B. Liu, H. Zhang, Y. Li, H. Zhou, H. Sun, W. Zhang, and Q. Zhao, "Relative humidity sensor based on tilted fiber Bragg grating with polyvinyl alcohol coating," IEEE Photonics Technol. Lett. **21**, 441–443 (2009).
30. J. Mathew, Y. Semenova, and G. Farrell, "Effect of coating length on the sensitivity of a humidity sensor based on an

Agarose coated photonic crystal fiber interferometer," Opt. Express **21**, 6313–6320 (2013).
31. C. A. Murray and J. R. Dutcher, "Effect of changes in relative humidity and temperature on ultrathin chitosan films," Biomacromolecules **7**, 3460–3465 (2006).
32. Y.-P. Miao, B. Liu, J. Liu, H. Sun, and Q.-D. Zhao, "Relative humidity sensor based on tilted fiber grating, " J. Optoelectron. Laser **21**, 978–982 (2010).